

REPORT DOCUMENTATION PAGE			Form Approved OMB NO. 0704-0188		
<p>The public reporting burden for this collection of information is estimated to average 1 hour per response, including the time for reviewing instructions, searching existing data sources, gathering and maintaining the data needed, and completing and reviewing the collection of information. Send comments regarding this burden estimate or any other aspect of this collection of information, including suggestions for reducing this burden, to Washington Headquarters Services, Directorate for Information Operations and Reports, 1215 Jefferson Davis Highway, Suite 1204, Arlington VA, 22202-4302. Respondents should be aware that notwithstanding any other provision of law, no person shall be subject to any penalty for failing to comply with a collection of information if it does not display a currently valid OMB control number.</p> <p>PLEASE DO NOT RETURN YOUR FORM TO THE ABOVE ADDRESS.</p>					
1. REPORT DATE (DD-MM-YYYY)		2. REPORT TYPE Technical Report		3. DATES COVERED (From - To) -	
4. TITLE AND SUBTITLE Optical Magnetism			5a. CONTRACT NUMBER W911NF-13-1-0473		
			5b. GRANT NUMBER		
			5c. PROGRAM ELEMENT NUMBER 611102		
6. AUTHORS			5d. PROJECT NUMBER		
			5e. TASK NUMBER		
			5f. WORK UNIT NUMBER		
7. PERFORMING ORGANIZATION NAMES AND ADDRESSES Purdue University Sponsored Program Services 155 S. Grant Street West Lafayette, IN 47907 -2114			8. PERFORMING ORGANIZATION REPORT NUMBER		
9. SPONSORING/MONITORING AGENCY NAME(S) AND ADDRESS (ES) U.S. Army Research Office P.O. Box 12211 Research Triangle Park, NC 27709-2211			10. SPONSOR/MONITOR'S ACRONYM(S) ARO		
			11. SPONSOR/MONITOR'S REPORT NUMBER(S) 64533-EL-II.1		
12. DISTRIBUTION AVAILABILITY STATEMENT Approved for public release; distribution is unlimited.					
13. SUPPLEMENTARY NOTES The views, opinions and/or findings contained in this report are those of the author(s) and should not be construed as an official Department of the Army position, policy or decision, unless so designated by other documentation.					
14. ABSTRACT Theoretical and numerical studies of metamaterials are addressing the question of whether true optical magnetism is possible. Lattice-based structures that have symmetries leading to unique descriptions of homogenized permeability are being evaluated. Current work on conduction current magnetism in carbon nanotubes is being extended to more general materials with consideration of displacement current effects. Numerical results are being viewed both in terms of spatial dispersion, associated with the structure of the material, and equivalent circuit concepts. Promising					
15. SUBJECT TERMS optics; materials; permeability					
16. SECURITY CLASSIFICATION OF:			17. LIMITATION OF ABSTRACT UU	15. NUMBER OF PAGES	19a. NAME OF RESPONSIBLE PERSON Kevin Webb
a. REPORT UU	b. ABSTRACT UU	c. THIS PAGE UU			19b. TELEPHONE NUMBER 765-494-3373

Report Title

Optical Magnetism

ABSTRACT

Theoretical and numerical studies of metamaterials are addressing the question of whether true optical magnetism is possible. Lattice-based structures that have symmetries leading to unique descriptions of homogenized permeability are being evaluated. Current work on conduction current magnetism in carbon nanotubes is being extended to more general materials with consideration of displacement current effects. Numerical results are being viewed both in terms of spatial dispersion, associated with the structure of the material, and equivalent circuit concepts. Promising results from this work will guide plans for an experimental demonstration of optical magnetism. Establishing that optical magnetism is possible would be of enormous importance, both in terms of the fundamental science, and also the myriad of applications that could be revolutionized by a magnetic metamaterial.

Progress Report for ARO Award W911NF-13-1-0473

Optical Magnetism

Kevin Webb Group
School of Electrical and Computer Engineering,
Purdue University, West Lafayette,
Indiana 47907, USA
webb@purdue.edu

for

Dr. William Clark, Army Research Office

(Dated: September 15, 2014)

Abstract

Theoretical and numerical studies of metamaterials are addressing the question of whether true optical magnetism is possible. Lattice-based structures that have symmetries leading to unique descriptions of homogenized permeability are being evaluated. Current work on conduction current magnetism in carbon nanotubes is being extended to more general materials with consideration of displacement current effects. Numerical results are being viewed both in terms of spatial dispersion, associated with the structure of the material, and equivalent circuit concepts. Promising results from this work will guide plans for an experimental demonstration of optical magnetism. Establishing that optical magnetism is possible would be of enormous importance, both in terms of the fundamental science, and also the myriad of applications that could be revolutionized by a magnetic metamaterial.

I. INTRODUCTION

In this report, we present the case for homogenized magnetism from arrays of carbon nanotube coils. There are existing fabrication methods for such coils, making the issue of the frequency range for significant permeability important and timely. We present a study of homogenization of LiNbO_3 (LN) and metallic structures to obtain the effective constitutive parameters from inversion of scattering parameters S_{21} and S_{11} [13]. The structures consist of periodically arranged lattice cells of dielectric or metallic patterns, with lattice constant on the order of $100\text{ }\mu\text{m}$ with a view to evaluation at terahertz frequencies in a scaled picture for optical magnetism. Scattering parameters (S_{11} and S_{21}) were obtained from finite-element (FEM) simulations of the structures with an incident monochromatic plane wave. A procedure for inverting these scattering parameters based on the formulation of Nicolson and Weir was applied to extract the homogenized constitutive parameters. Over the frequency involved in the study, the effective wavelength in the structure remained larger than about 10 times the crystal periodicity, which justifies the homogenization. The results indicate that both paramagnetic and diamagnetic responses can be achieved through structured patterning of LN as well as in metallic structures. We took into consideration the fact that most metamaterials are anisotropic and exhibit chirality, and investigated the dispersion relations of plane wave propagation in chiral (bi-isotropic) and the more general bianisotropic media. The plan for subsequent studies includes an extension of the S-parameter homogenization method to allow the extraction of the full tensor components of $\bar{\epsilon}_r$, $\bar{\mu}_r$, and in addition the chirality parameter tensor $\bar{\kappa}$.

II. MAGNETISM FROM CARBON NANOTUBE COIL ARRAYS

Our preliminary studies suggest that THz and perhaps optical magnetism is possible with carbon nanocoil mixtures which have been fabricated, and that we may be able to achieve a resonance in the infrared spectral regime. Our results that are being prepared for submission to a journal are summarized here.

Carbon nanotubes (CNTs) and nanowires (CNWs) have been the subject of intense research in the last couple of decades because of their unusual mechanical and electrical properties. In the last decade, interest in more exotic nanostructures such as CNW rings and

coils has evolved both due to academic curiosity and to the great potential such structures hold in electrical and mechanical applications [2, 4, 6, 14, 25]. However, while it has been known for some time that growing nanotubes and nanowires in increased ambient entropy (achieved by ultrasonic and microwave chemical-vapor deposition (CVD), or injection of sublimated compounds) results in coiling [9, 10], the necessary understanding and technology has only recently matured to a level where such nanostructures can be synthesized [1]. This understanding stems from a unified thermodynamic model that explains the coiling using the energy minimization principle. This model, together with recent technological improvements [11, 23, 24] in the CVD synthesis of coils, paves the way to achieving coils with high yield and high precision at increasingly small coil dimensions (see Fig. 1). Those achievements lead us to believe that a volume containing small enough nanocoils at a high enough density for use as an effective medium may produce negative permeability at THz and perhaps some optical frequency ranges, and that this could be manufactured using today's CVD-based methods.

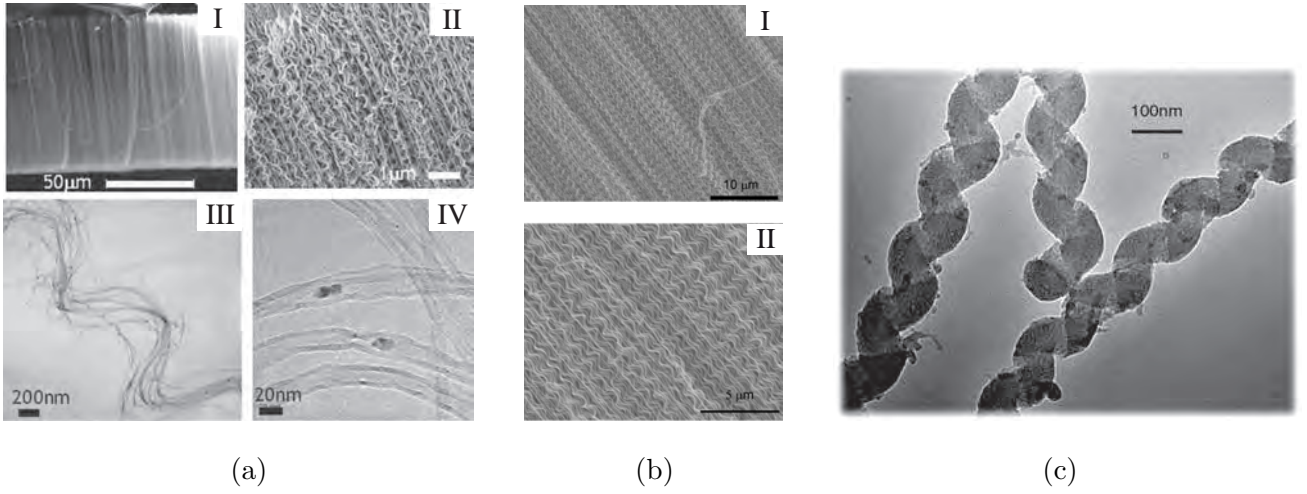


FIG. 1. (a) [I & II] Low and high magnification scanning electron microscopy (SEM) pictures showing an as-grown forest of coil-shaped carbon nanotubes (CCNT) synthesized by use of thermal CVD with a bi-metal catalyst formed from a mixture of ferrocene and indium isopropoxide as coiling seed. [III & IV] Low and high magnification transmission electron microscopy (TEM) images of a loose single bundle of coil-shaped carbon nanotubes (from [3]). (b) [I & II] SEM pictures of coiled features of CCNTs synthesized via CVD from pyridine and sublimated melamine injection (from [11]). (c) TEM picture of carbon CCNTs synthesized via microwave CVD with fine Ni particles as catalyst (from [22]).

Before studying the effective electromagnetic parameters of a volume containing a multi-

tude of nanocoils, it is important to pay attention to the subtle issue of chirality. Most metamaterials exhibit only simple constitutive relations of the form $\mathbf{D} = \epsilon_0 \bar{\epsilon} \cdot \mathbf{E}$ and $\mathbf{B} = \mu_0 \bar{\mu} \cdot \mathbf{H}$, where \mathbf{E} and \mathbf{H} are the electric and magnetic fields, respectively, \mathbf{D} and \mathbf{B} are the electric and magnetic flux densities, respectively, ϵ_0 and μ_0 are the free-space permittivity and permeability, respectively, and $\bar{\epsilon}$ and $\bar{\mu}$ are the effective relative permittivity and permeability dyadics of the metamaterial, respectively. However, coils are asymmetric with respect to mirror reflection, which means that a substance comprising coils could be chiral, and hence exhibit more complicated bi-anisotropic constitutive relations of the form

$$\mathbf{D} = \epsilon_0 \bar{\epsilon} \cdot \mathbf{E} - j\sqrt{\mu_0 \epsilon_0} \bar{\kappa}^T \cdot \mathbf{H} \quad \mathbf{B} = j\sqrt{\mu_0 \epsilon_0} \bar{\kappa} \cdot \mathbf{E} + \mu_0 \bar{\mu} \cdot \mathbf{H}, \quad (1)$$

where $\bar{\kappa}$ is the chirality parameter dyadic relating the magnetic field to the electric flux and vice versa [18]. While the design and application of chiral materials has been thoroughly studied during the last decade of the 20th century, this work had the goal of attaining chirality [17]. On the other hand, we are interested in suppressing chirality while retaining the large local magnetic effect of each coil. By doing so, it is possible to obtain a simple effective medium whose quasi-static resonance will have a large enough influence on the effective permeability to drive its values into the negative range. The quasi-static resonance is due to the inductance of the coil and the capacitance between coil turns. In order to suppress chirality, we suggest a cellular structure where each cell comprises a single coil, and each pair of neighboring cells are of different handedness (i.e., left-hand and right-hand coils, as in Fig. 2(a)). This structure will be on average symmetric with respect to mirror reflection, and thus non-chiral. To obtain an initial estimate of the effective properties of such a structure, we studied the homogenized permeability of a super cell of 8 CNW coils, shown in Fig. 2(b), in a doubly periodic lattice. We used a vector electromagnetic solution and a parameter extraction procedure similar to the one used in [19], as a function of material thickness, in order to establish converged bulk parameters. To simplify our initial calculations and obtain results that are dependent only on the ratio between dimensions and wave-length, we used classical graphite properties for the coils and assumed a small skin depth compared with coil wire thickness. This simplification allowed us to concentrate on the choice of coil and cell dimensions that will decrease the resonant frequency while keeping the coil to coil interaction weak, so that the effective medium parameters will converge even for small material thickness. The result in Fig. 2(c) shows the real and imaginary components of the homogenized permeability as having a resonance, and that it is a metamaterial. It

would therefore appear that a mixture of CNT coils could provide negative μ at THz and perhaps optical frequencies with an appropriate geometry. We also found that the resonant frequency in the homogenized result is insensitive to source polarization and orientation, which is very important for random mixtures.

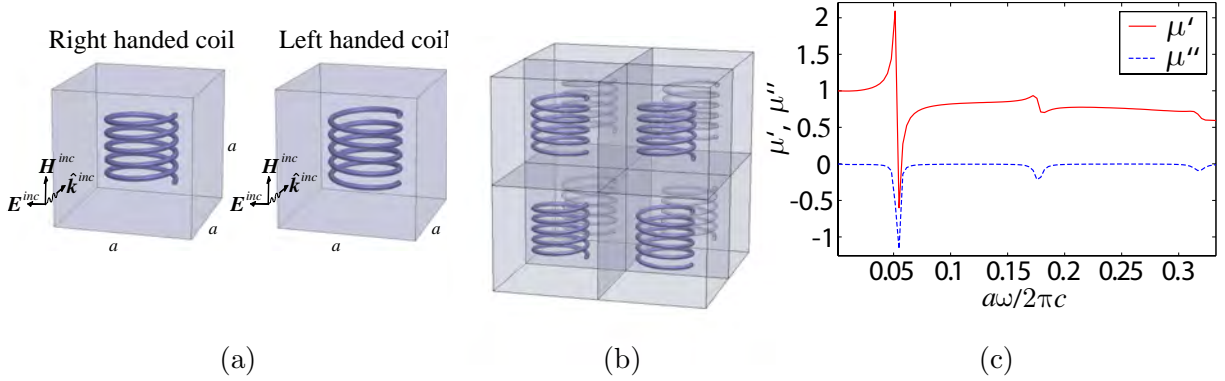


FIG. 2. (a) Left-handed and right-handed carbon coils that are placed in $a \times a \times a$ cells. The coil diameter and length is $0.5a$, and the wire diameter is $0.02a$. (b) Non-chiral unit-cell of periodic metamaterial that comprises 4 left-handed coils and 4 right-handed coils. (c) Real (μ') and imaginary (μ'') components of the effective permeability of the coil metamaterial, obtained using a scattering model.

A more accurate approximation of the performance of CNT coils is obtained by modeling the tubes with a surface conductivity given by the Landauer formula for a quantum conductor

$$g_{s,\text{tube}} = \frac{G_0 M L_0}{2\pi R}, \quad (2)$$

where G_0 is the conductance quantum, M is the number of modes carried by the wire, L_0 is the mean free path length in the wire, and R is the tube radius. Based on the scaling principle, it can be shown that the resonance frequency is independent of the surface conductivity value, and the CNT coil effective permeability can be accurately predicted by a simple Lorentzian resonance model in the angular frequency ω ,

$$\mu = 1 + \frac{\Delta\mu\omega^2}{\omega_0^2 - \omega^2 + j2\gamma\omega}, \quad (3)$$

that is fitted for the dipole strength $\Delta\mu$, the resonance angular frequency ω_0 , and the damping coefficient γ . Figure 3 shows the effective permeability obtained from full-wave simulations and by the model in (3). Within the regime of weak interaction between coil elements, the coefficients of the model in (3) have a simple dependency on geometrical properties of

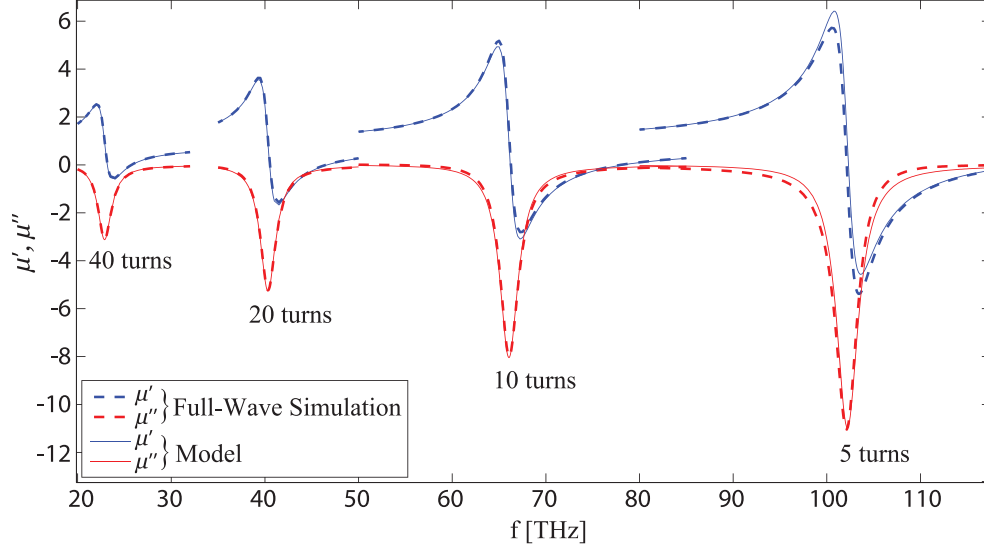


FIG. 3. Real (μ') and imaginary (μ'') components of the effective permeability of a coil metamaterial based on an improved tube model for coils with different number of turns. The dashed plots are obtained using scattering parameters extracted from full-wave simulations and the solid plots are obtained from the resonance model in (3). The unit-cell geometry used in the simulations consists of a 50 nm diameter coil with a 16 nm pitch that is set in the middle of a unit-cell box that is constantly kept 1.5 times the size of the coil in all dimensions. The surface conductivity of the coil is based on the Landauer formula in (2) with $M = 2$ modes, a mean free path length of $L_0 = 150\mu\text{m}$, and tube radius of $R = 0.5\text{nm}$

the tube, and can give invaluable insights into the physics governing the CNT coil-based metamaterial performance. The model can also be used to decouple the design process of CNT coil-based metamaterials from the CNT conductance properties that, for frequencies above low THz, are still under active scientific investigation in the carbon nanotube research community.

An aspect of importance for the applicability of nanocoil based metamaterials is their loss tangent. While all resonant based metamaterials exhibit some degree of loss, our calculations show that this loss is not necessarily significant in the frequency in which the effective permeability of a nanocoil based medium is negative. It is interesting to note that while some have shown that substances comprising carbon nanotubes can behave as a dark material, it is mainly due to a specific choice of effective medium parameters so as to suppress the substance's reflectance, while the effective absorption length of such substances is actually

very long [5].

Figure 4 shows the dependency of the extracted resonance parameters on the number of modes in the Landauer equation (2) for different relative unit-cell sizes (given by α). This plot shows that the conductivity plays a major role only in the resonance dumping coefficient and, in general for small conductivities (as expected from Born approximation), the overall effect on the magnetic susceptibility (χ in the lower right panel) is linear. This observation reaffirms the prediction, based on the scaling principle, that the resonance frequency of the coil mixture is mainly a function of the geometrical properties of the unit-cell while being almost independent of the coil conductivity.

Figure 5 shows the extracted resonance model parameters as a function of the number of coil turns (two upper panels), and as a function of the resonance frequency (two lower panels). The middle panel shows the resonance frequency as a function of the number of coil turns and can be seen as connecting between the two upper panels and the two lower panels. Three curves are plotted in each panel for three different relative unit-cell sizes. The linear dependence of the curves in the upper-right, middle and lower-left panels as the number of coil turns becomes large (or resonance frequency becomes small) can be used for simple linear extrapolation (important since we are interested in the THz frequency range - below 10 THz) that is shown as a continuation of the curves as dashed lines. The linear extrapolation of the upper-right and lower-left panels can be used to find the extrapolation of the curves in the lower-right and upper-left, respectively, based on the relation between coil turns and resonance frequency shown in the middle panel. This connection between the extrapolated plots in different panels is illustrated in the figure by the two yellow curved arrows, beginning with the panels where extrapolation is linear and crossing through the middle panel to translate turns to resonance frequency (and vice-versa), in order to find the extrapolation at the panels where the arrows end. The linear curves for a large number of coil turns (or small resonance frequency) can help provide understanding of the nature of the relationship between those values and the resonance properties.

Figure 6 shows the peak-to-peak variation of the magnetic susceptibility (maximum minus the minimum of the real part) normalized for the surface conductivity of one conductance quantum as a function of the resonance frequency for different relative unit-cell sizes. Such plots are meaningful because of the linear effect of conductivity shown in Fig. 4. Again, due to the linearity of the curves for low frequencies, it possible to extrapolate them down to the

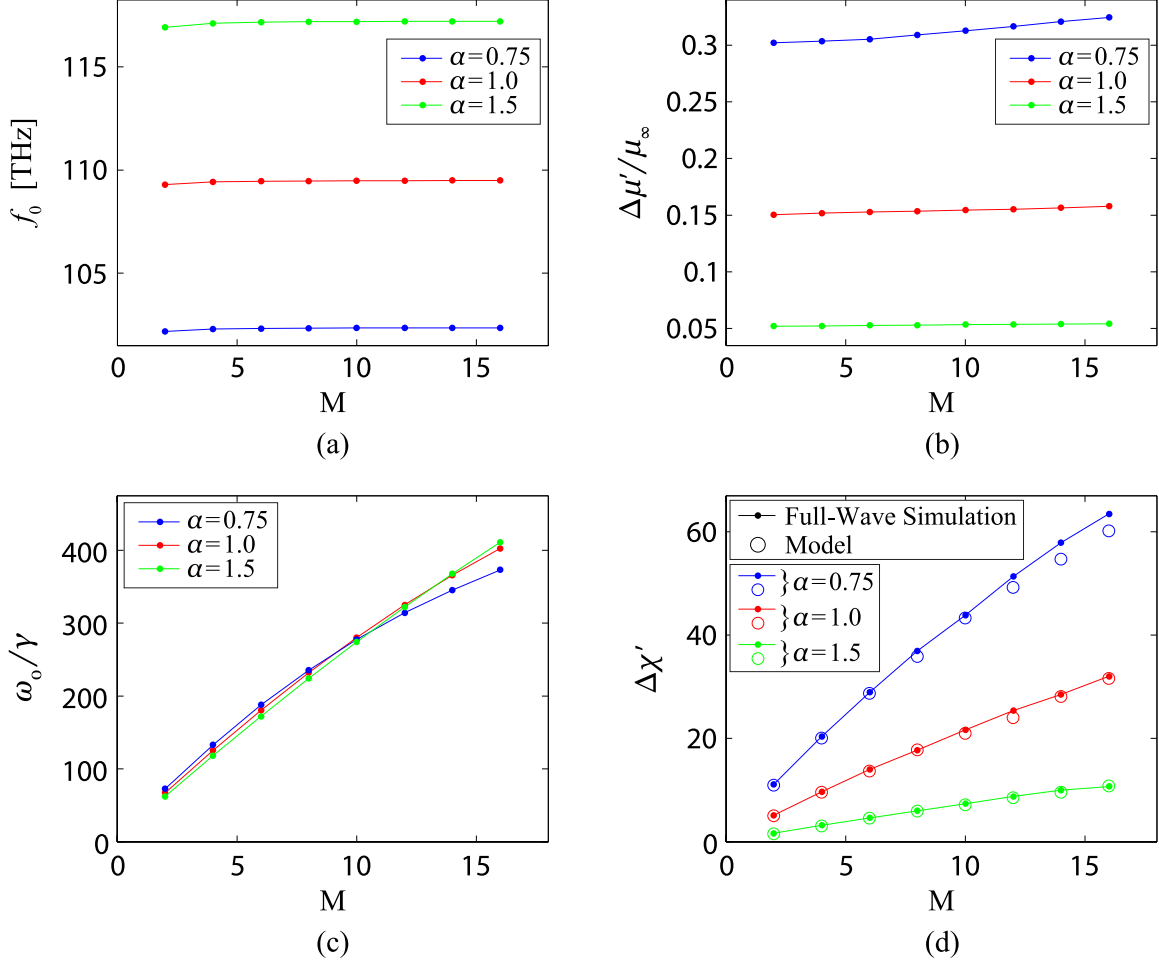


FIG. 4. Extracted parameters of the permeability resonance model as a function of the number of modes in the Landauer equation for different relative unit-cell sizes (given by α); (a) resonance frequency, (b) dipole strength, (c) damping coefficient, (d) peak-to-peak variance in magnetic susceptibility. In panel (d), the dot-marked curves show the results as obtained from the numerical simulation, while the circle markers indicate the results as obtained from the fitted resonance model.

THz frequency range. This plot can be used to predict the magnetic susceptibility based on a desired resonant frequency and unit-cell size, for a given surface conductivity, in units of conductance quanta.

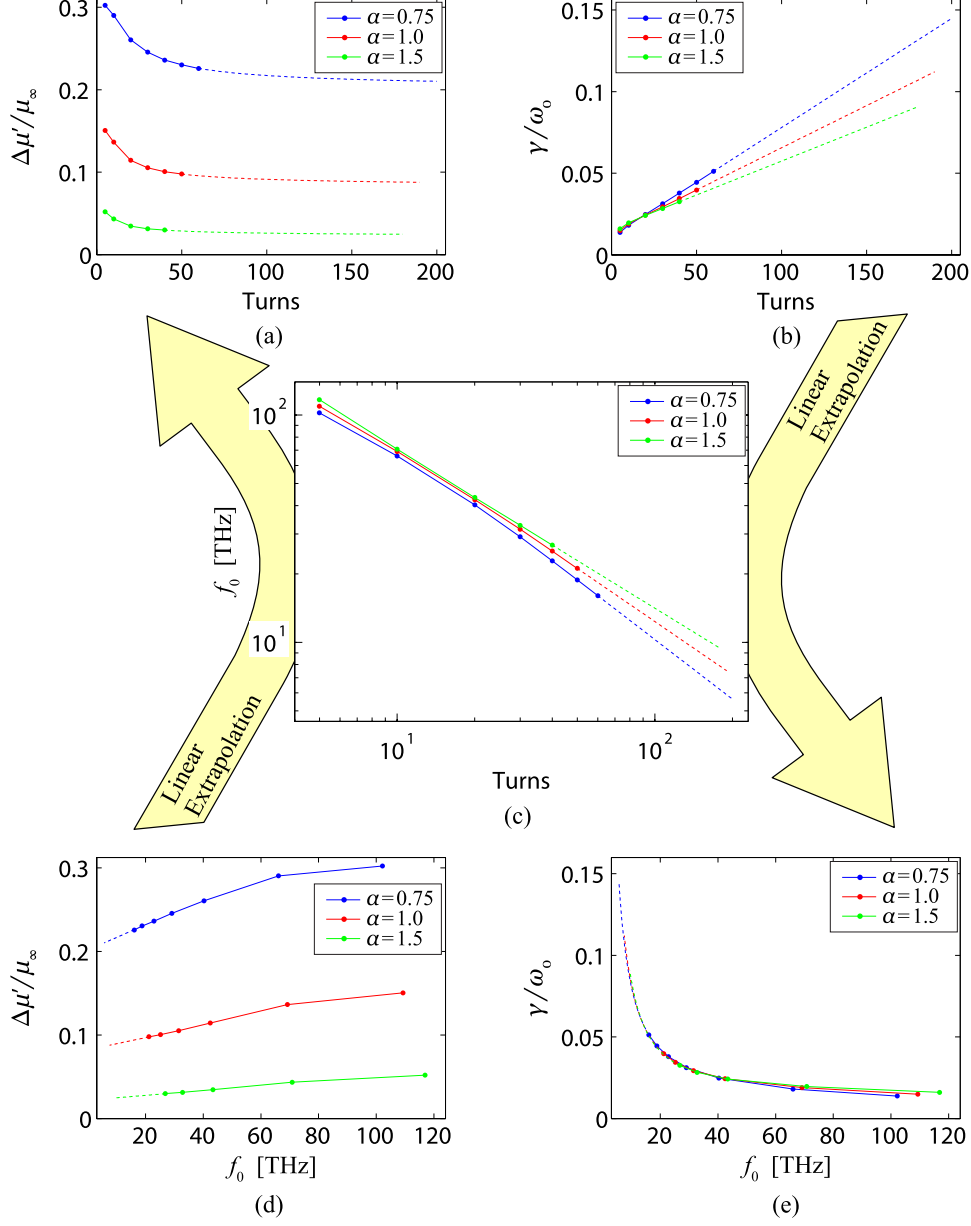


FIG. 5. Dependence of the extracted resonance model parameters on the number of turns in the coils (two upper and middle panels), and on the resonance frequency (two lower panels).

III. LITHIUM NIOBATE (LN) WITH CIRCULARLY ARRANGED VACUUM HOLES

Because displacement current will be key to achieving optical magnetism, we consider a structured dielectric material that should provide insight. We chose LiNbO_3 - LN for this initial work because it has a large dielectric constant and because it can be laser machined

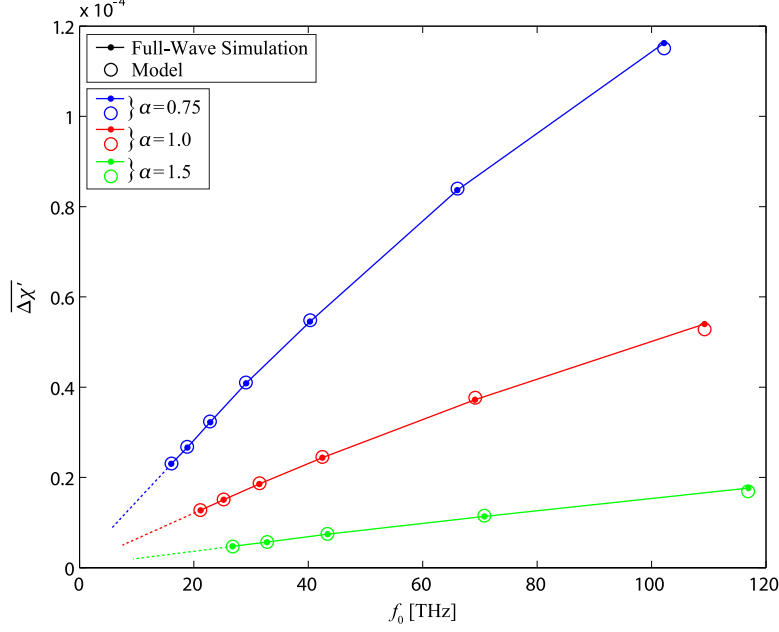


FIG. 6. Peak-to-peak variation of the magnetic susceptibility normalized for the surface conductivity of one conductance quantum as a function of the resonance frequency for different relative unit-cell sizes. The dashed curves show the results as obtained from the numerical simulation, while the circle markers indicate the results obtained from the fitted resonance model.

for scaled THz measurements and imaged using light. This could and would be done in collaboration with Prof. Keith Nelson’s group at MIT.

We present the numerical studies of extracted homogenized constitutive parameters ϵ_r and μ_r from structured LN. These extracted complex parameters are given as functions of frequency. The structure under study consists of periodically arranged rings of vacuum holes in a background of LN. Each unit cell measures $120 \mu\text{m}$ in width and $100 \mu\text{m}$ in height. In each unit cell, seven vacuum holes are located on a circle of $30 \mu\text{m}$ radius, equally spaced. A vacuum hole measures $5 \mu\text{m}$ in radius. The structure is evident in the electric field plot of Fig. 7(a).

We investigated the homogenized electromagnetic response of the structure in the frequency range between 0.03 THz and 0.3 THz. At 0.194 THz, the wavelength in the LN background is $\lambda_{\text{LiNbO}_3} = 240 \mu\text{m}$, twice the periodicity of the crystal structure, which results in significant reflection (Fig. 7 b). Frequency regimes meaningful to homogenization should be lower than the first crystal mode, and in order for the effective wavelength to be greater than 10 times the structure period, the frequency ought to be lower than 0.039 THz.

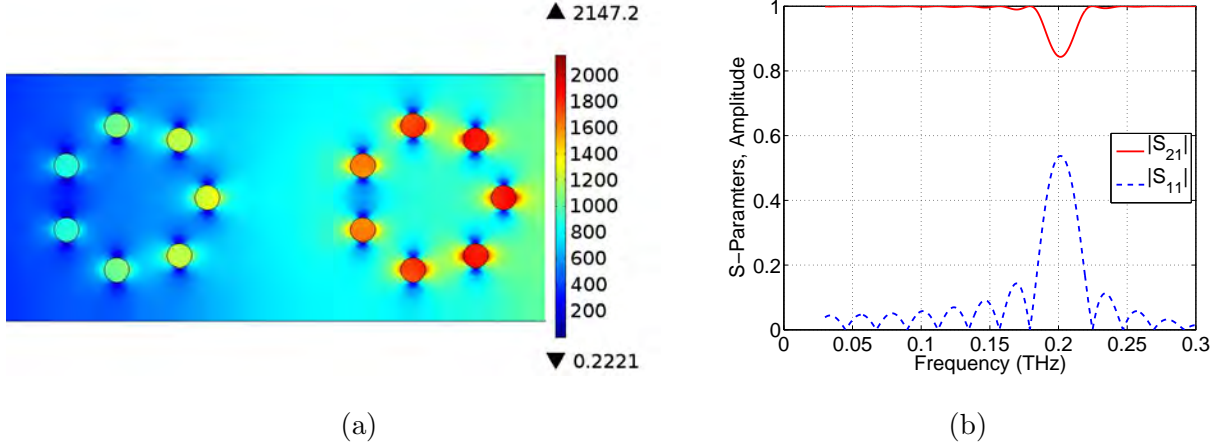


FIG. 7. (a) The in-plane component of total E-field (incident plus scattered), over the spatial extent of two unit cells. A TM-polarized plane wave (\mathbf{H} out of the page) at 0.03 THz is incident from the left. Each unit cell is composed of a circular array of holes in LN. The entire structure under study consists of nine such unit cells. Shown in the plot is a region over two unit cells. (b) Magnitudes of the transmission (S_{21}) and reflection (S_{11}) coefficients for an array of holes in LN. The first crystal mode lies at around 0.2 THz. The structure under study consists of 9 unit cells. Each unit cell is composed of a circular array of holes in LN.

The effective constitutive parameters were obtained using the Nicolson-Ross-Weir method [13], and are given in Fig. 8. Notice that for frequencies substantially below the resonance (0.194 THz) that μ_r approaches unity, but also that the values in this example may still be useful in applications (see Fig. 8(d)). The point of this example is the develop understanding of magnetism based on displacement current (with positive real part of the dielectric constant) that could be translated to optical frequencies. This result suggests further exploration of the relation between the geometry and homogenized magnetic response should prove interesting.

IV. COMPLEMENTARY STRUCTURE 1: CIRCULARLY ARRANGED LITHIUM NIOBATE (LN) RODS IN VACUUM BACKGROUND

The homogenized extraction results for complementary structures having dielectric rods in free space are presented. The complementary structure to that used in Fig. 7 was obtained by replacing the LN background with vacuum, and the vacuum holes in the structure by LN

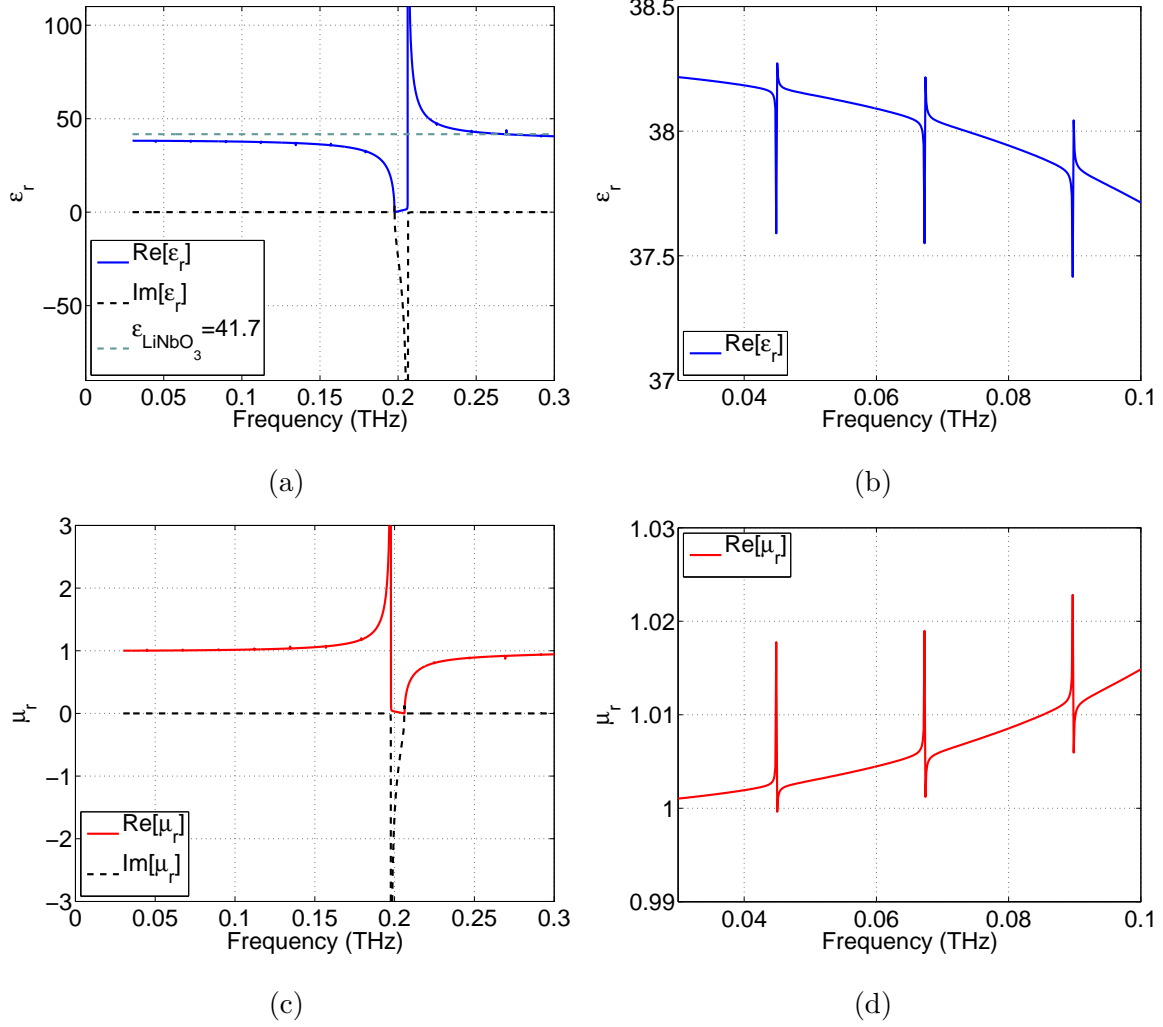


FIG. 8. Homogenized results for holes in LN. (a) Extracted relative permittivity ϵ_r over the frequency range 0.03 ~ 0.3 THz. (b) ϵ_r at frequencies below 0.1 THz. (c) Extracted relative permittivity μ_r over the frequency range 0.03 ~ 0.3 THz. (d) μ_r at frequencies below 0.1 THz.

rods. Also, the radius of the rods was increased from 5 μm to 10 μm . The reduced distance between rods increases the coupling and enhances the ability of the structure to scatter incoming waves. The reduction in background refractive index enlarges the frequency range meaningful for homogenization. Based on the effective wavelength in the structure being limited to be no less than 10 times the period ($\lambda \geq 10\Lambda$), we estimate that meaningful homogenization can only be carried out at frequencies lower than 0.25 THz. Numerical scattering parameter magnitude data is provided in Fig. 9. The extracted homogenized responses are given in Fig. 10. The fine features in the extracted effective constitutive parameters are shown in the magnified plots of Fig. 11. Significant deviations from unity

have been achieved in the homogenized effective magnetic response μ_r , which are largely diamagnetic. Note that the deviation of μ_r from unity is larger in Fig. 11(b) than for the complementary structure of holes in LN (Fig. 8(d)).

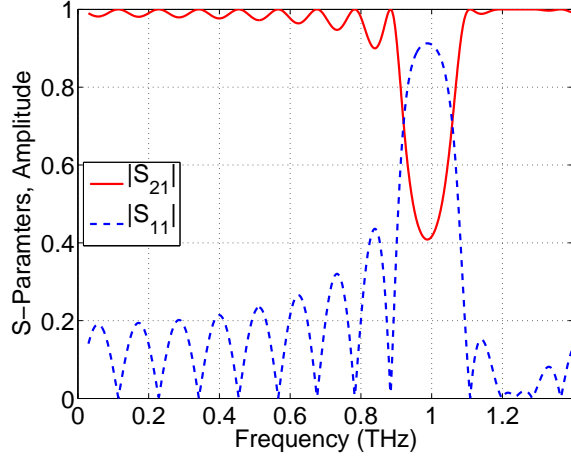


FIG. 9. Magnitude of the S-Parameters for a unit cell composed of a circular array of LN rods, showing the first crystal mode at around 1 THz. The structure consists of nine unit cells. Each unit cells is made up of a circular arrangement of seven LN rods.

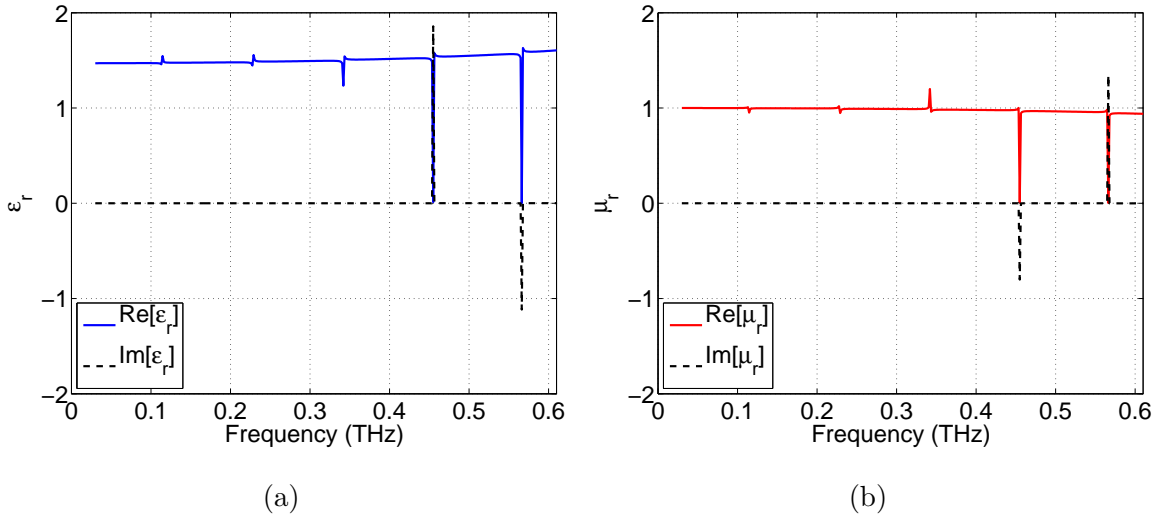


FIG. 10. Homogenized response for the complementary structure (LN rods in free space) and the data in Fig. 9. (a) Effective relative permittivity ϵ_r over the frequency range 0.03 ~ 0.6 THz. Both real and imaginary parts are shown in the plot. (b) Effective relative permeability μ_r over the frequency range 0.03 ~ 0.6 THz. Both real and imaginary parts are shown in the plot.

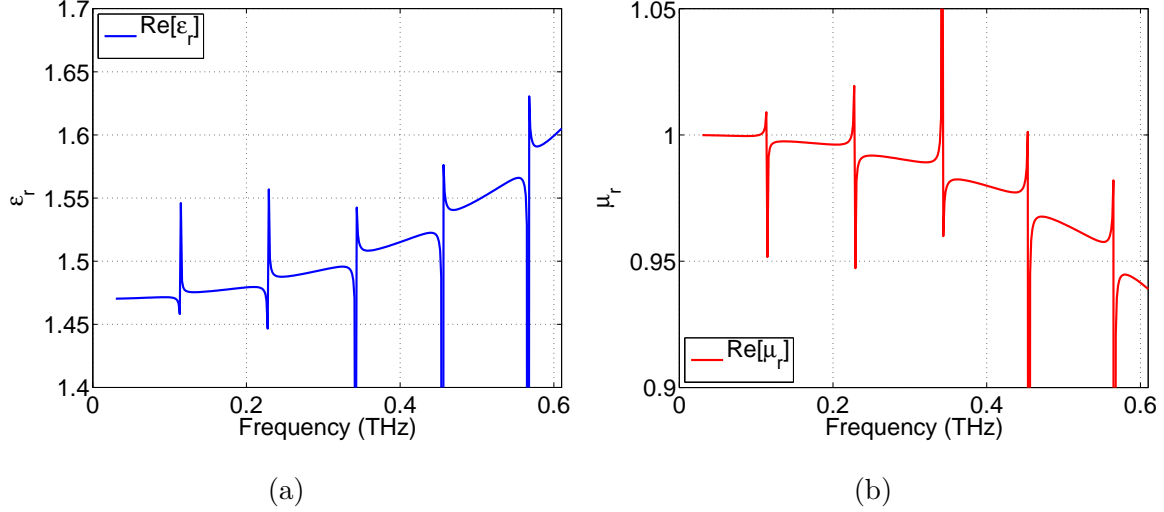


FIG. 11. Expanded scales for the results in Fig. 10 for LN rods. (a) Real part of the effective relative permittivity ϵ_r over the frequency range 0.03 ~ 0.6 THz. (b) Real part of the effective relative permeability μ_r over the frequency range 0.03 ~ 0.6 THz. The structure under study consists of nine unit cells. Each unit cell is made up of a circular arrangement of seven LN rods.

V. COMPLEMENTARY STRUCTURE 2: CIRCULARLY ARRANGED METALLIC RODS IN A VACUUM BACKGROUND

The effect of replacing dielectric components (LN) with metallic elements (having negative real part of the dielectric constant) was investigated. The structure under investigation has the same unit cell and periodicity as the complementary structure in the previous section. In a vacuum background, each unit cell had a circular arrangement of metal rods. Each rod was 10 μm in radius. The metal was a hypothetical material having permittivity $\epsilon_r = -41.7$. A field solution is given in Fig. 12 and the calculated scattering parameter magnitudes as a function of frequency in Fig. 13. The extracted parameters, ϵ_r and μ_r , are plotted as functions of frequency in Fig. 14. We expect the homogenization to be meaningful at frequencies below 0.25 THz. The effective magnetic response is mostly diamagnetic, having $\mu_r < 1$. Note that the deviation of μ_r from unity is similar in Fig. 14(b), where $\epsilon_r < 0$, to that for the material having the same geometry but with $\epsilon_r > 0$ in Fig. 11(b). The relationship between magnetism and the sign of the dielectric constant of the composing material needs to be investigated further. The fact that we achieve similar magnetism independent of the sign of the real part of the material dielectric constant could be quite important.

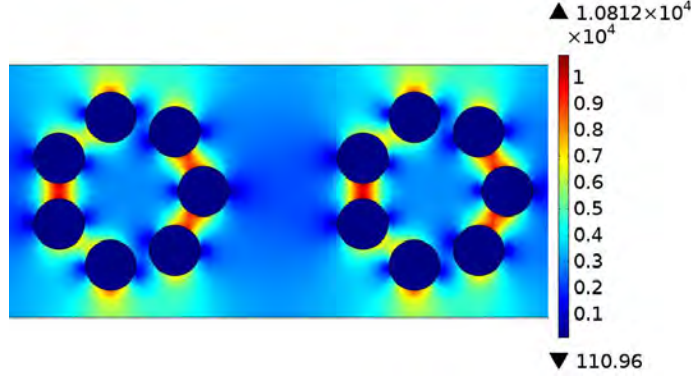


FIG. 12. Metal rods in free space ($\epsilon_r = -41.7$). Plot of the in-plane component of E-field. A TM-polarized plane wave at 0.03 THz is incident from the left. At this frequency, the wavelength in the background is 1 cm, significantly larger than the size of the unit cell $120 \mu\text{m}$. Each metal rod has radius of $10 \mu\text{m}$. The entire structure under study consists of nine unit cells.

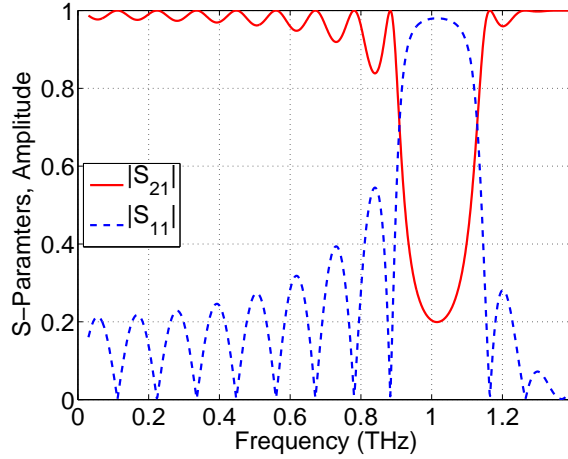


FIG. 13. Amplitude of S-Parameters, showing the first crystal mode at around 1 THz.

VI. A COMPARISON OF DIELECTRIC AND METALLIC STRUCTURES UNDER TE-POLARIZED INCIDENCE

The extracted material parameters, ϵ_r and μ_r , are plotted for the same dielectric and metallic structures that were covered in the previous two sections, but with TE polarization. With a change of incident plane wave polarization to TE, we were able to probe the other tensor components of the constitutive parameters, allowing investigation of differences between the two complementary structures having LN rods and metal rods, although under TM incidence, the effective parameters extracted from the two structures were almost

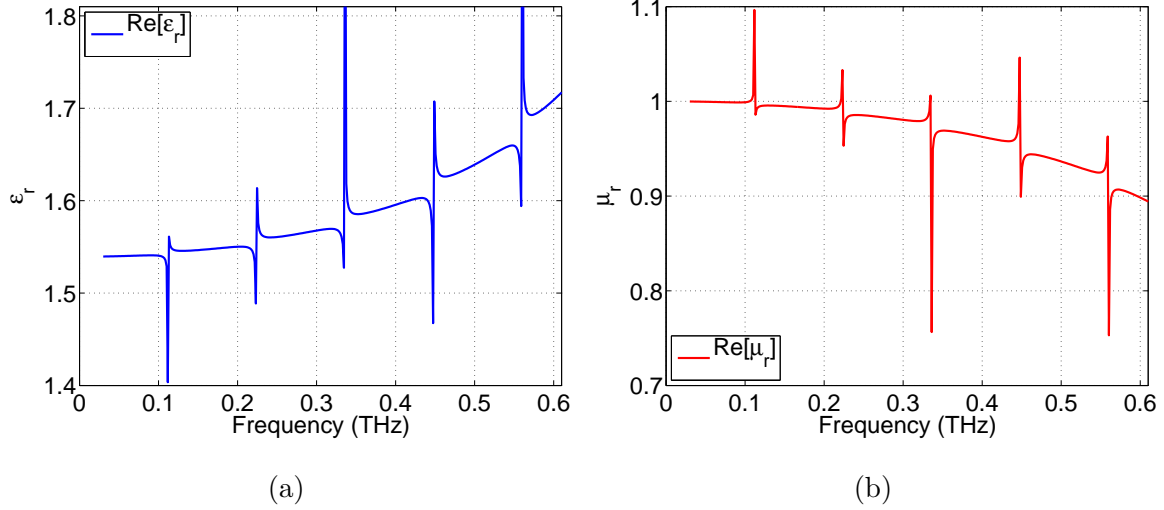


FIG. 14. Homogenization with metal rods in free space ($\epsilon_r = -41.7$) for TM. (a) Real part of the effective relative permittivity ϵ_r over the frequency range $0.03 \sim 0.6$ THz. (b) Real part of the effective relative permeability μ_r over the frequency range $0.03 \sim 0.6$ THz. The structure under study consists of nine unit cells. Each unit cells is made up of a circular arrangement of seven metallic rods.

identical.

In Fig. 15, the S-parameters of these two structures are plotted. The incident plane wave has TE polarization, with the electric field vector oriented parallel to the rods. Overall, the metallic structure demonstrates much stronger reflection, and heavy attenuation of forward propagating waves than does the LN structure. These differences in scattering characteristics lead to very dissimilar effective medium parameters, as shown in Fig. 16. For the dielectric structure, Fig. 16(a) shows $\epsilon_r > 1$, whereas we find $\epsilon_r < 1$ for the metallic case, as shown in Fig. 16(b). The results agree with predictions based on Maxwell-Garnett mixing theory.

The extracted magnetic responses show significant deviation from unity, as plotted in Fig. 17. However, we need to consider more general constitutive relations. While spatial dispersions can give rise to magnetism, we should be careful in reviewing the results of Fig. 17 because the electric field (normal to the page) does not link the magnetic flux, except at infinity. The extracted response should in fact be interpreted in terms of the chirality tensor, which highlights the necessity of incorporating material chirality or bianisotropy into the extraction methods. We note that the inclusions in this structure do not exhibit any handedness, and are in fact non-chiral. However, such a lack of chirality in the microstructure

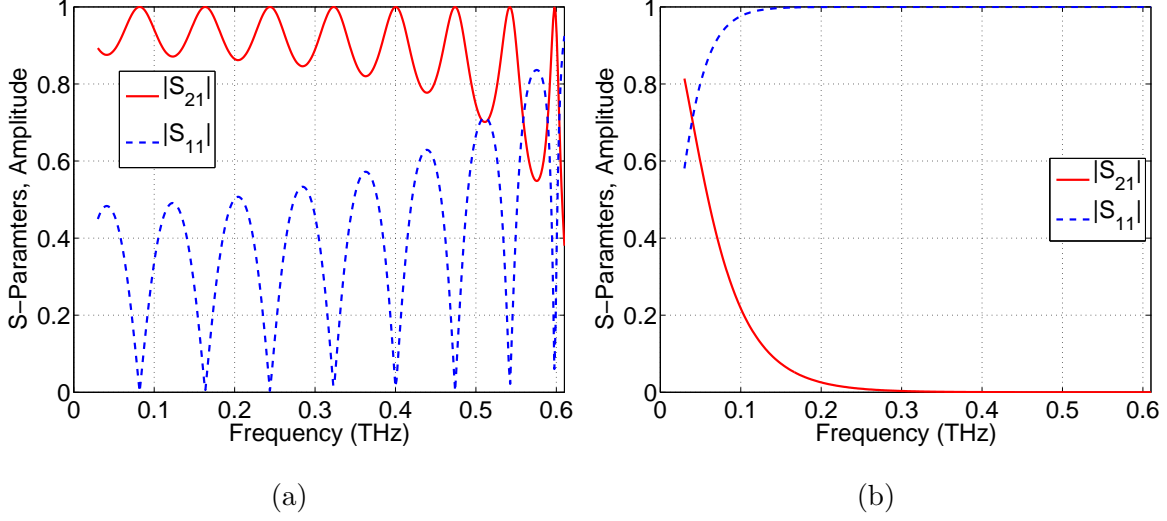


FIG. 15. (a) Magnitude of S-parameters for the complementary structure having LN rods. (b) Magnitude of the S-parameters for the complementary structure having metal rods. Both structures consist of nine unit cells with the same cell dimension.

does not preclude magneto-electric coupling and could provide homogenized parameters with non-zero entries in a general chirality tensor [17]. In the two sections that follow, we derive aspects of plane wave propagation in isotropic chiral media and the more general bianisotropic media, in anticipation of future work on extraction methods that takes into account these general constitutive tensors.

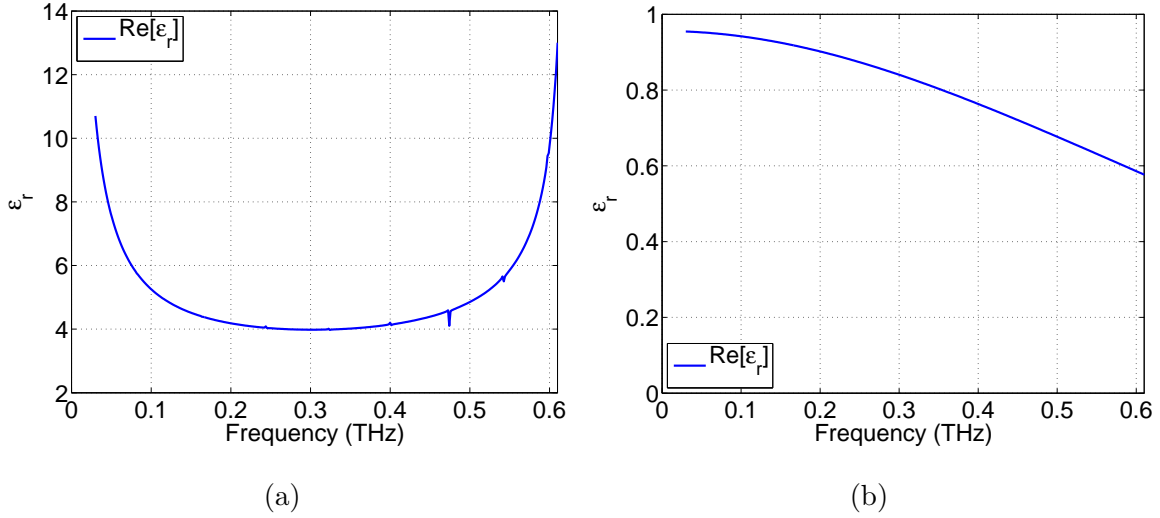


FIG. 16. Under TE incidence, the extracted effective permittivities are plotted for (a) LN structure ($\epsilon_r = 41.7$ rods) and (b) metallic structure ($\epsilon_r = -41.7$ rods). Both structures consist of nine unit cells with the same cell dimension.

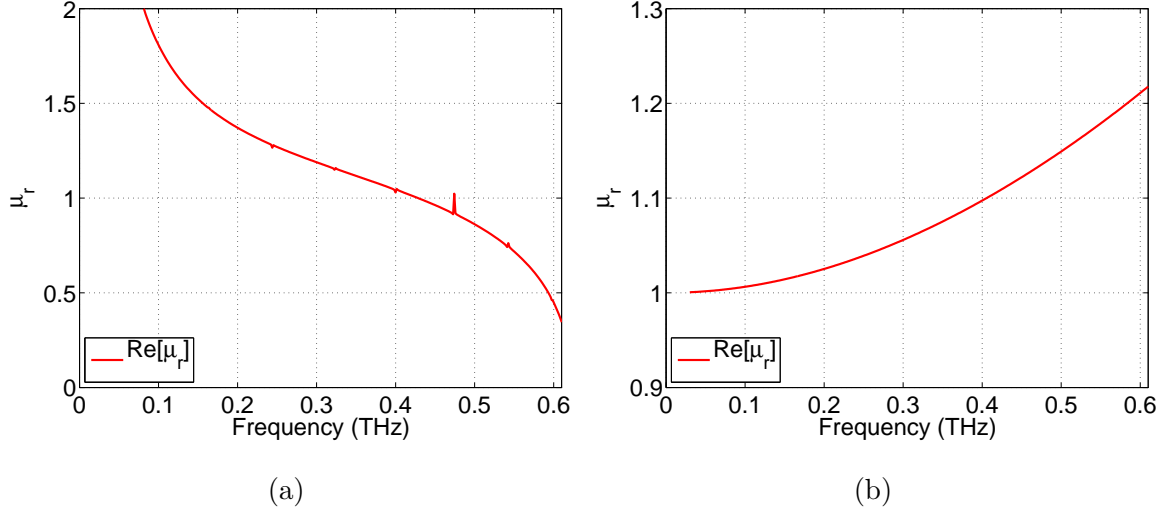


FIG. 17. Extracted effective permeabilities for (a) LN structure ($\epsilon_r = 41.7$ rods) and (b) metallic structure ($\epsilon_r = -41.7$ rods). Both structures consist of nine unit cells with the same cell dimension.

VII. PLANE WAVE PROPAGATION IN ISOTROPIC CHIRAL MEDIA

Evaluation of magnetic material properties requires attention to the material symmetry, leading to the constitutive relations. Given these, the dispersion relation yields insight into wave propagation in the material. This picture is developed here and will be used in future work with the development of extraction methods incorporating chirality tensor and anisotropy.

The plane wave eigenvalue or dispersion surface problem in relation to various material tensors (and related to material symmetry) is developed here. While not unique, we write $\mathbf{D} = f(\mathbf{E}, \mathbf{H})$ and $\mathbf{B} = f(\mathbf{E}, \mathbf{H})$. From Maxwell's equations, this has a fundamental basis, because \mathbf{J} drives \mathbf{H} , for example, and \mathbf{B} is a result of the material properties, given \mathbf{H} . This picture is quite pervasive, at least in the classical field literature. However, because the homogenized constitutive parameter relations are invertible, the specific form ($\mathbf{D} = f(\mathbf{E}, \mathbf{H})$ and $\mathbf{B} = f(\mathbf{E}, \mathbf{H})$ or $\mathbf{E} = f(\mathbf{D}, \mathbf{B})$ and $\mathbf{H} = f(\mathbf{D}, \mathbf{B})$) is largely irrelevant, it would seem. Therefore, and equivalently, one can say that \mathbf{H} is the result of material properties, given \mathbf{B} .

Consider the bi-anisotropic constitutive relations of the form

$$\mathbf{D} = \epsilon_0 \bar{\epsilon} \cdot \mathbf{E} - j\sqrt{\mu_0 \epsilon_0} \bar{\kappa}^T \cdot \mathbf{H} \quad (4)$$

$$\mathbf{B} = j\sqrt{\mu_0 \epsilon_0} \bar{\kappa} \cdot \mathbf{E} + \mu_0 \bar{\mu} \cdot \mathbf{H}, \quad (5)$$

where $\bar{\epsilon}$ is the dielectric constant tensor, $\bar{\mu}$ is the relative permeability tensor, $\bar{\kappa}$ is the chirality parameter tensor relating the magnetic field to the electric flux and vice versa, and $\exp(j\omega t)$ time dependence has been assumed [17]. The form of (4) and (5) implies linear and reciprocal media, and is convenient in the solution of wave propagation problems. This is equivalent to what has been called the Post relations (see page 26 of [17]). The crystal symmetry dictates the form of the tensors in (4) and (5) - see Chapter 6 of [17], for example.

Removal of chirality in (4) and (5), by introducing appropriate cell boundary conditions of through appropriate mixtures leads to a straight forward interpretation of $\bar{\epsilon}$ and $\bar{\mu}$ from scattering experiments on a slab of this material, as we have described [12]. However, from suitable measurements for TE and TM polarization, all the constitutive elements are uniquely available. This means that the possibility of optical magnetism can be investigated through optical scattering measurements.

Consider the simplified isotropic and chiral constitutive relations

$$\mathbf{D} = \epsilon_0 \epsilon \mathbf{E} + j \frac{\kappa}{c} \mathbf{H} \quad (6)$$

$$\mathbf{B} = -j \frac{\kappa}{c} \mathbf{E} + \mu_0 \mu \mathbf{H}. \quad (7)$$

In (6) and (7), ϵ , μ and κ are unitless, and using SI units, ϵ_0 has units F/m, and μ_0 has units H/m. The units for \mathbf{D} are C/m², for \mathbf{E} are V/m, for \mathbf{H} are A/m, and for \mathbf{B} are T (or Wb/m²).

For a plane wave with spatial variation $\exp(-j\mathbf{k} \cdot \mathbf{r})$, Maxwell's equations become

$$\mathbf{k} \times \mathbf{H} = -\omega \mathbf{D} \quad (8)$$

$$\mathbf{k} \times \mathbf{E} = \omega \mathbf{B} \quad (9)$$

$$\mathbf{k} \cdot \mathbf{D} = 0 \quad (10)$$

$$\mathbf{k} \cdot \mathbf{B} = 0. \quad (11)$$

Note that the reason the constitutive relations in (4) and (5) are particularly useful is that can be directly substituted into the right hand sides of (8) and (9). A forward model to describe the scattering parameters of a homogenized slab also directly use this form, and

this can be used in conjunction with measurements to extract the constitutive parameters (and evidence of magnetism) [12].

For a plane wave with $\exp(-j\mathbf{k} \cdot \mathbf{r})$ spatial dependency, the operation $\nabla \times$ is equivalent to $-j\mathbf{k} \times$, and with $\mathbf{k} = k_x\hat{x} + k_y\hat{y} + k_z\hat{z}$, we can write

$$\mathbf{k} \times = \begin{bmatrix} 0 & -k_z & k_y \\ k_z & 0 & -k_x \\ -k_y & k_x & 0 \end{bmatrix}. \quad (12)$$

Using (12), we can write

$$\mathbf{k} \times \mathbf{k} \times = \begin{bmatrix} -k_y^2 - k_z^2 & k_x k_y & k_x k_z \\ k_x k_y & -k_y^2 - k_z^2 & k_y k_z \\ k_x k_z & k_y k_z & -k_x^2 - k_y^2 \end{bmatrix}. \quad (13)$$

From (9), the Helmholtz wave equation is formed as

$$\mathbf{k} \times \mathbf{k} \times \mathbf{E} = \omega \mathbf{k} \times \mathbf{B}, \quad (14)$$

and substituting (7) and then (6) leads to

$$\begin{aligned} \mathbf{k} \times \mathbf{k} \times \mathbf{E} &= \omega \mathbf{k} \times \left(-j\frac{\kappa}{c}\mathbf{E} + \mu_0\mu\mathbf{H} \right) \\ &= -j\omega\frac{\kappa}{c}\mathbf{k} \times \mathbf{E} + \omega\mu_0\mu(-\omega\mathbf{D}) \\ &= -j\omega\frac{\kappa}{c}\mathbf{k} \times \mathbf{E} - \omega^2\mu_0\mu \left(\epsilon_0\epsilon\mathbf{E} + j\frac{\kappa}{c}\mathbf{H} \right) \\ &= -j\omega^2\frac{\kappa}{c} \left(-j\frac{\kappa}{c}\mathbf{E} + \mu_0\mu\mathbf{H} \right) - \omega^2\mu_0\mu \left(\epsilon_0\epsilon\mathbf{E} + j\frac{\kappa}{c}\mathbf{H} \right) \end{aligned} \quad (15)$$

where (9) and (7) were used to obtain the last equation in (15). Equation (15) leads to

$$\mathbf{k} \times \mathbf{k} \times \mathbf{E} + k_0^2 (\mu\epsilon + \kappa^2) \mathbf{E} + j2\omega^2\frac{\kappa}{c}\mu_0\mu\mathbf{H} = 0. \quad (16)$$

Starting with (8), we have

$$\mathbf{k} \times \mathbf{k} \times \mathbf{H} = -\omega \mathbf{k} \times \mathbf{D}, \quad (17)$$

and substituting (6) and then (7) leads to

$$\begin{aligned} \mathbf{k} \times \mathbf{k} \times \mathbf{H} &= -\omega \mathbf{k} \times \left(\epsilon_0\epsilon\mathbf{E} + j\frac{\kappa}{c}\mathbf{H} \right) \\ &= -\omega\epsilon_0\epsilon\mathbf{k} \times \mathbf{E} - j\omega\frac{\kappa}{c}\mathbf{k} \times \mathbf{H} \\ &= -\omega^2\epsilon_0\epsilon \left(-j\frac{\kappa}{c}\mathbf{E} + \mu_0\mu\mathbf{H} \right) - j\omega\frac{\kappa}{c}\mathbf{k} \times \mathbf{H} \\ &= -\omega^2\epsilon_0\epsilon \left(-j\frac{\kappa}{c}\mathbf{E} + \mu_0\mu\mathbf{H} \right) + j\omega^2\frac{\kappa}{c} \left(-j\frac{\kappa}{c}\mathbf{E} + \mu_0\mu\mathbf{H} \right). \end{aligned} \quad (18)$$

Equation (18) leads to

$$\mathbf{k} \times \mathbf{k} \times \mathbf{H} + k_0^2 (\mu\epsilon + \kappa^2) \mathbf{H} - j2\omega^2 \epsilon_0 \epsilon \frac{\kappa}{c} \mathbf{E} = 0. \quad (19)$$

Let $k_x = 0$ and $k_y = 0$, i.e., consider normal incidence, a substantial restriction but a simplifying assumption. Using (16) and (19),

$$\mathbf{\Lambda} \cdot \begin{bmatrix} E_x \\ E_y \\ H_x \\ H_y \end{bmatrix} = 0, \quad (20)$$

where from (13)

$$\mathbf{\Lambda} = \begin{bmatrix} -k^2 + k_0^2 \mu \epsilon + k_0^2 \kappa^2 & 0 & j2\omega^2 \mu_0 \mu \frac{\kappa}{c} & 0 \\ 0 & -k^2 + k_0^2 \mu \epsilon + k_0^2 \kappa^2 & 0 & j2\omega^2 \mu_0 \mu \frac{\kappa}{c} \\ -j2\omega^2 \epsilon_0 \epsilon \frac{\kappa}{c} & 0 & -k^2 + k_0^2 \mu \epsilon + k_0^2 \kappa^2 & 0 \\ 0 & -j2\omega^2 \epsilon_0 \epsilon \frac{\kappa}{c} & 0 & -k^2 + k_0^2 \mu \epsilon + k_0^2 \kappa^2 \end{bmatrix} \quad (21)$$

We modify (20), so that all sub-matrices have the same units, choosing

$$\mathbf{\Lambda}' \cdot \begin{bmatrix} E_x \\ E_y \\ \eta_0 H_x \\ \eta_0 H_y \end{bmatrix} = 0, \quad (22)$$

where $\eta_0 = \sqrt{\mu_0/\epsilon_0}$ is the free space wave impedance with units of Ω and

$$\mathbf{\Lambda}' = \begin{bmatrix} -k^2 + k_0^2 (\mu\epsilon + \kappa^2) & 0 & j2\kappa \mu k_0^2 & 0 \\ 0 & -k^2 + k_0^2 (\mu\epsilon + \kappa^2) & 0 & j2\kappa \mu k_0^2 \\ -j2\kappa \mu k_0^2 & 0 & -k^2 + k_0^2 (\mu\epsilon + \kappa^2) & 0 \\ 0 & -j2\kappa \mu k_0^2 & 0 & -k^2 + k_0^2 (\mu\epsilon + \kappa^2) \end{bmatrix} \quad (23)$$

All entries in (23) have the same units. The dispersion relation (DR) we seek is $\det \mathbf{\Lambda}' = 0$.

We can use the identity

$$\det \begin{bmatrix} A & B \\ -C & D \end{bmatrix} = \det A \det(D + CA^{-1}B) \quad (24)$$

$$= \det D \det(A + BD^{-1}C) \quad (25)$$

or other analytical methods to evaluate the determinant of (23) and find

$$(\det \mathbf{\Lambda}')^{1/2} = \left(\Lambda'_{11}{}^2 - \Lambda'_{13} \Lambda'_{31} \right)^2 \quad (26)$$

$$= k^4 - 2k_0^2 k^2 (\mu\epsilon + \kappa^2)^2 + k_0^4 (\mu\epsilon - \kappa^2)^2 \quad (27)$$

$$= 0. \quad (28)$$

Solving (28) as a quadratic equation gives

$$\frac{k^2}{k_0^2} = \mu\epsilon + \kappa^2 \pm (2\kappa\sqrt{\mu\epsilon}) \quad (29)$$

$$= n^2, \quad (30)$$

where n is the (complex) refractive index. Consequently,

$$n = \sqrt{\mu\epsilon} \pm \kappa. \quad (31)$$

which is the basis of chirality leading to a negative refractive index [15]. However, the specific relationship of the two characteristic solutions to the polarization must be considered. The two solutions (n_{\pm}) have been assigned to right and left-handed circularly polarized eigenstates [16], attributed to [20]. A treatment in terms of wave fields indicates that those are circularly polarized and have the refractive indices in (31) [21].

In the case of circular polarization, $\mathbf{E} = E_0(\hat{x} + j\hat{y})$ for RHCP and $\mathbf{E} = E_0(\hat{x} - j\hat{y})$ for LHCP. We can thus write $E_y = pE_x$ with $p = j$ for RHCP and $p = -j$ for LHCP, for example. When $|p| \neq 1$, the polarization state is in general elliptical (linear being a special case). Consider here an electric field basis for polarization, i.e., use of $\mathbf{E}(t)$). However, \mathbf{D} has been used [8], where, incidentally, $\mathbf{E} = f(\mathbf{D}, \mathbf{B})$ and $\mathbf{H} = f(\mathbf{D}, \mathbf{B})$ has been employed. The description of $\mathbf{D}(t)$ and $\mathbf{E}(t)$ differ in general.

To evaluate the polarization, consider (8) and (9) with the constitutive relations in (6) and (7). With $\kappa = 0$ and isotropic material, the eigenvalues for k are identical and E_x and E_y are independent. However, with $\kappa \neq 0$, the situation differs. Writing the components of (8) and (9), with $\mathbf{k} = k\hat{z}$, and rearranging, gives

$$kH_y = \omega\epsilon_0\epsilon E_x + j\frac{\omega\kappa}{c}H_x \quad (32)$$

$$kH_x = -\omega\epsilon_0\epsilon E_y - j\frac{\omega\kappa}{c}H_y \quad (33)$$

$$kE_y = j\frac{\omega\kappa}{c}E_x - \omega\mu_0\mu H_x \quad (34)$$

$$kE_x = -j\frac{\omega\kappa}{c}E_y + \omega\mu_0\mu H_y, \quad (35)$$

Arranging (32) - (35) into matrix form yields [7]

$$\begin{bmatrix} -k & -j\omega\kappa/c \\ -j\omega\kappa/c & k \end{bmatrix} \begin{bmatrix} E_x \\ E_y \end{bmatrix} = - \begin{bmatrix} 0 & \omega\mu_0\mu \\ \omega\mu_0\mu & 0 \end{bmatrix} \begin{bmatrix} H_x \\ H_y \end{bmatrix} \quad (36)$$

$$\begin{bmatrix} -k & -j\omega\kappa/c \\ -j\omega\kappa/c & k \end{bmatrix} \begin{bmatrix} H_x \\ H_y \end{bmatrix} = \begin{bmatrix} 0 & \omega\epsilon_0\epsilon \\ \omega\epsilon_0\epsilon & 0 \end{bmatrix} \begin{bmatrix} E_x \\ E_y \end{bmatrix}. \quad (37)$$

Eliminating the magnetic field results in

$$\begin{bmatrix} -j2k_0k\kappa & k^2 + k_0^2\kappa^2 - k_0^2\mu\epsilon \\ k^2 + k_0^2\kappa^2 - k_0^2\mu\epsilon & j2k_0k\kappa \end{bmatrix} \begin{bmatrix} E_x \\ E_y \end{bmatrix} = \begin{bmatrix} 0 \\ 0 \end{bmatrix}. \quad (38)$$

By setting the determinant of the coefficient matrix in (38), $k/k_0 = n = \sqrt{\mu\epsilon} \pm \kappa$, consistent with (31). Substituting for k in (38) leads to

$$\frac{E_x}{E_y} = \pm j \quad \text{for} \quad n = \sqrt{\mu\epsilon} \pm \kappa, \quad (39)$$

i.e., $+\kappa$ yields RHCP and $-\kappa$ corresponds to LHCP. This result is independent of the sign of κ and holds for complex μ , ϵ , and κ .

Consider now the wave field transformations [21] that allow

$$\mathbf{D}_{\pm} = \epsilon\epsilon_0\mathbf{E} + j\frac{\kappa}{c}\mathbf{H} = \epsilon_{\pm}\epsilon_0\mathbf{E}_{\pm} \quad (40)$$

$$\mathbf{B}_{\pm} = \mu\mu_0\mathbf{H} - j\frac{\kappa}{c}\mathbf{E} = \mu_{\pm}\mu_0\mathbf{H}_{\pm}, \quad (41)$$

which are provided for with [21]

$$\mathbf{E} = \mathbf{E}_+ + \mathbf{E}_- \quad (42)$$

$$j\eta\mathbf{H} = \mathbf{E}_+ - \mathbf{E}_- \quad (43)$$

$$\mathbf{H} = \mathbf{H}_+ + \mathbf{H}_- \quad (44)$$

$$\frac{j}{\eta}\mathbf{E} = \mathbf{H}_+ - \mathbf{H}_-, \quad (45)$$

where $\eta = \eta_0\sqrt{\mu/\epsilon}$, with η_0 the free space wave impedance. In this case,

$$\epsilon_{\pm} = \epsilon\epsilon_0(1 \pm \kappa_r) \quad (46)$$

$$\mu_{\pm} = \mu\mu_0(1 \pm \kappa_r), \quad (47)$$

where $\kappa_r = \kappa/\sqrt{\mu\epsilon}$, and an equivalent non-chiral medium has been achieved. Therefore, the refractive index is again given by (31). The eigenmodes \mathbf{E}_+ , \mathbf{H}_+ and \mathbf{E}_- , \mathbf{H}_- have been described as right hand and left hand circularly polarized [21].

VIII. PLANE WAVES IN UNIAXIAL BIANISOTROPIC MEDIA

In preparation for developing extraction methods that incorporate more general constitutive tensors, we consider now the description of plane waves in media that have both anisotropy and magneto-electric coupling. This description will be important for many nanostructured materials that could display optical magnetism.

We consider reciprocal bianisotropic media described by uniaxial material dyadics [17]. Physically, this means that there is only one preferred direction in space defined by the geometry and the positions of inclusions or molecules. The time convention taken here is $\exp(j\omega t)$. The most general form of constitutive relations allowed under such conditions are

$$\mathbf{D} = \bar{\bar{\epsilon}} \cdot \mathbf{E} - j\sqrt{\epsilon_0\mu_0}(\kappa_t \bar{\bar{I}}_t + \kappa_n \hat{\mathbf{z}}\hat{\mathbf{z}} - K \bar{\bar{J}}) \cdot \mathbf{H} \quad (48)$$

$$\mathbf{B} = \bar{\bar{\mu}} \cdot \mathbf{H} + j\sqrt{\epsilon_0\mu_0}(\kappa_t \bar{\bar{I}}_t + \kappa_n \hat{\mathbf{z}}\hat{\mathbf{z}} - K \bar{\bar{J}}) \cdot \mathbf{E}, \quad (49)$$

where the permittivity $\bar{\bar{\epsilon}}$ and permeability $\bar{\bar{\mu}}$ are uniaxial dyadics given by

$$\bar{\bar{\epsilon}} = \epsilon_0(\epsilon_t \bar{\bar{I}}_t + \epsilon_n \hat{\mathbf{z}}\hat{\mathbf{z}}), \quad \bar{\bar{\mu}} = \mu_0(\mu_t \bar{\bar{I}}_t + \mu_n \hat{\mathbf{z}}\hat{\mathbf{z}}) \quad (50)$$

and

$$\bar{\bar{I}}_t = \begin{bmatrix} 1 & 0 & 0 \\ 0 & 1 & 0 \\ 0 & 0 & 0 \end{bmatrix}, \quad \hat{\mathbf{z}}\hat{\mathbf{z}} = \begin{bmatrix} 0 & 0 & 0 \\ 0 & 0 & 0 \\ 0 & 0 & 1 \end{bmatrix}, \quad \bar{\bar{J}} = \hat{\mathbf{z}} \times \bar{\bar{I}}_t = \begin{bmatrix} 0 & -1 & 0 \\ 1 & 0 & 0 \\ 0 & 0 & 0 \end{bmatrix}. \quad (51)$$

The cross product is to be understood as

$$\mathbf{a} \times \mathbf{b} = \begin{bmatrix} 0 & -a_3 & a_2 \\ a_3 & 0 & -a_1 \\ -a_2 & a_1 & 0 \end{bmatrix} \begin{bmatrix} b_1 \\ b_2 \\ b_3 \end{bmatrix}. \quad (52)$$

Therefore, (48) and (49) expand into

$$\begin{bmatrix} D_x \\ D_y \\ D_z \end{bmatrix} = \begin{bmatrix} \epsilon_t & 0 & 0 \\ 0 & \epsilon_t & 0 \\ 0 & 0 & \epsilon_n \end{bmatrix} \cdot \begin{bmatrix} E_x \\ E_y \\ E_z \end{bmatrix} - j\sqrt{\epsilon_0\mu_0} \begin{bmatrix} \kappa_t & K & 0 \\ -K & \kappa_t & 0 \\ 0 & 0 & \kappa_n \end{bmatrix} \cdot \begin{bmatrix} H_x \\ H_y \\ H_z \end{bmatrix} \quad (53)$$

$$\begin{bmatrix} B_x \\ B_y \\ B_z \end{bmatrix} = \begin{bmatrix} \mu_t & 0 & 0 \\ 0 & \mu_t & 0 \\ 0 & 0 & \mu_n \end{bmatrix} \cdot \begin{bmatrix} H_x \\ H_y \\ H_z \end{bmatrix} + j\sqrt{\epsilon_0\mu_0} \begin{bmatrix} \kappa_t & -K & 0 \\ K & \kappa_t & 0 \\ 0 & 0 & \kappa_n \end{bmatrix} \cdot \begin{bmatrix} E_x \\ E_y \\ E_z \end{bmatrix}. \quad (54)$$

The antisymmetric elements in the magnetoelectric (chiral) dyadic arise from “hat”-inclusions [17], with the axes oriented along the z -axis. In the formulation of Eqs. (53) and (54), we have taken the optic axis of the uniaxial medium to be the z -axis. Note that Ref. [17], page 28, provides a proof (to be verified) that Eqs. (53) and (54) satisfy Lorentz reciprocity. We decompose the fields as

$$\mathbf{E} = \mathbf{E}_t + E_n \hat{\mathbf{z}}, \quad \mathbf{H} = \mathbf{H}_t + H_n \hat{\mathbf{z}} \quad (55)$$

We take the two-dimensional Fourier transform of the two Maxwell curl equations in the transverse (xy -) plane, so that

$$\nabla \times \square = -j \begin{bmatrix} 0 & -\frac{\partial}{\partial z} & k_y \\ \frac{\partial}{\partial z} & 0 & -k_x \\ -k_y & k_x & 0 \end{bmatrix} \cdot \square, \quad \frac{\partial \square}{\partial t} = j\omega \square. \quad (56)$$

Maxwell’s curl equations then become

$$-j \begin{bmatrix} 0 & -\frac{\partial}{\partial z} & k_y \\ \frac{\partial}{\partial z} & 0 & -k_x \\ -k_y & k_x & 0 \end{bmatrix} \begin{bmatrix} E_x \\ E_y \\ E_z \end{bmatrix} = -j\omega \begin{bmatrix} \mu_t & 0 & 0 \\ 0 & \mu_t & 0 \\ 0 & 0 & \mu_n \end{bmatrix} \begin{bmatrix} H_x \\ H_y \\ H_z \end{bmatrix} + k_0 \left(\begin{bmatrix} \kappa_t E_x \\ \kappa_t E_y \\ \kappa_n E_z \end{bmatrix} + K \begin{bmatrix} -E_y \\ E_x \\ 0 \end{bmatrix} \right) \quad (57)$$

$$-j \begin{bmatrix} 0 & -\frac{\partial}{\partial z} & k_y \\ \frac{\partial}{\partial z} & 0 & -k_x \\ -k_y & k_x & 0 \end{bmatrix} \begin{bmatrix} H_x \\ H_y \\ H_z \end{bmatrix} = j\omega \begin{bmatrix} \epsilon_t & 0 & 0 \\ 0 & \epsilon_t & 0 \\ 0 & 0 & \epsilon_n \end{bmatrix} \begin{bmatrix} E_x \\ E_y \\ E_z \end{bmatrix} + k_0 \left(\begin{bmatrix} \kappa_t H_x \\ \kappa_t H_y \\ \kappa_n H_z \end{bmatrix} - K \begin{bmatrix} -H_y \\ H_x \\ 0 \end{bmatrix} \right), \quad (58)$$

where $k_0 = \omega\sqrt{\epsilon_0\mu_0}$ is the free-space wavenumber. Carrying out the matrix-vector multiplications gives

$$\begin{aligned} -j \begin{bmatrix} -\frac{\partial E_y}{\partial z} + k_y E_z \\ \frac{\partial E_x}{\partial z} - k_x E_z \\ -k_y E_x + k_x E_y \end{bmatrix} &= -j\omega \begin{bmatrix} \mu_t H_x & 0 & 0 \\ 0 & \mu_t H_y & 0 \\ 0 & 0 & \mu_n H_z \end{bmatrix} + k_0 \begin{bmatrix} \kappa_t E_x - K E_y \\ \kappa_t E_y + K E_x \\ \kappa_n E_z \end{bmatrix} \\ -j \begin{bmatrix} -\frac{\partial H_y}{\partial z} + k_y H_z \\ \frac{\partial H_x}{\partial z} - k_x H_z \\ -k_y H_x + k_x H_y \end{bmatrix} &= j\omega \begin{bmatrix} \epsilon_t E_x & 0 & 0 \\ 0 & \epsilon_t E_y & 0 \\ 0 & 0 & \epsilon_n E_z \end{bmatrix} + k_0 \begin{bmatrix} \kappa_t H_x + K H_y \\ \kappa_t H_y - K H_x \\ \kappa_n H_z \end{bmatrix}. \end{aligned} \quad (59)$$

After eliminating the normal field components, E_z and H_z , (59) can be written as a system

of two equations in the transverse field components as (see page 175 of Ref. [17])

$$\left\{ \begin{bmatrix} \frac{\partial}{\partial z} - k_0 K & 0 & 0 \\ 0 & \frac{\partial}{\partial z} - k_0 K & 0 \\ 0 & 0 & 0 \end{bmatrix} + \begin{bmatrix} \kappa_t k_0 & 0 & 0 \\ 0 & \kappa_t k_0 & 0 \\ 0 & 0 & 0 \end{bmatrix} + \frac{\kappa_n}{k_0(\epsilon_n \mu_n - \kappa_n^2)} \begin{bmatrix} k_x k_x & k_x k_y & 0 \\ k_y k_x & k_y k_y & 0 \\ 0 & 0 & 0 \end{bmatrix} \right\} \begin{bmatrix} 0 & -1 & 0 \\ 1 & 0 & 0 \\ 0 & 0 & 0 \end{bmatrix} \begin{bmatrix} E_x \\ E_y \\ 0 \end{bmatrix} \\ = \begin{pmatrix} \begin{bmatrix} \mu_t & 0 & 0 \\ 0 & \mu_t & 0 \\ 0 & 0 & 0 \end{bmatrix} - \frac{j\eta_0 \mu_n}{k_0(\epsilon_n \mu_n - \kappa_n^2)} \begin{bmatrix} k_x k_x & k_x k_y & 0 \\ k_y k_x & k_y k_y & 0 \\ 0 & 0 & 0 \end{bmatrix} \end{pmatrix} \begin{bmatrix} -H_y \\ H_x \\ 0 \end{bmatrix} \quad (60)$$

$$\left\{ \begin{bmatrix} \frac{\partial}{\partial z} + k_0 K & 0 & 0 \\ 0 & \frac{\partial}{\partial z} + k_0 K & 0 \\ 0 & 0 & 0 \end{bmatrix} + \begin{bmatrix} 0 & -1 & 0 \\ 1 & 0 & 0 \\ 0 & 0 & 0 \end{bmatrix} \left(\begin{bmatrix} \kappa_t k_0 & 0 & 0 \\ 0 & \kappa_t k_0 & 0 \\ 0 & 0 & 0 \end{bmatrix} + \frac{\kappa_n}{k_0(\epsilon_n \mu_n - \kappa_n^2)} \begin{bmatrix} k_x k_x & k_x k_y & 0 \\ k_y k_x & k_y k_y & 0 \\ 0 & 0 & 0 \end{bmatrix} \right) \right\} \begin{bmatrix} -H_y \\ H_x \\ 0 \end{bmatrix} \\ = \begin{pmatrix} \begin{bmatrix} \epsilon_t & 0 & 0 \\ 0 & \epsilon_t & 0 \\ 0 & 0 & 0 \end{bmatrix} - \frac{j\epsilon_n}{k_0 \eta_0 (\epsilon_n \mu_n - \kappa_n^2)} \begin{bmatrix} k_y k_y & -k_y k_x & 0 \\ -k_x k_y & k_x k_x & 0 \\ 0 & 0 & 0 \end{bmatrix} \end{pmatrix} \begin{bmatrix} E_x \\ E_y \\ 0 \end{bmatrix} \quad (61)$$

Substituting (60) into (61), it is possible to eliminate the magnetic field and yields the second-order wave equation for the transverse electric field components $E_t = [E_x \ E_y \ 0]^T$ as

$$\left(\frac{a_{11}}{k_t^2} \begin{bmatrix} k_x k_x & k_y k_y & 0 \\ k_y k_x & k_y k_y & 0 \\ 0 & 0 & 0 \end{bmatrix} + \frac{a_{22}}{k_t^2} \begin{bmatrix} k_y k_y & -k_y k_x & 0 \\ -k_x k_y & k_x k_x & 0 \\ 0 & 0 & 0 \end{bmatrix} + \frac{a_{12}}{k_t^2} \begin{bmatrix} -k_x k_y & k_x k_x & 0 \\ -k_y k_y & k_y k_x & 0 \\ 0 & 0 & 0 \end{bmatrix} + \frac{a_{21}}{k_t^2} \begin{bmatrix} -k_y k_y & -k_y k_y & 0 \\ k_x k_x & k_x k_y & 0 \\ 0 & 0 & 0 \end{bmatrix} \right) \begin{bmatrix} E_x \\ E_y \\ 0 \end{bmatrix} = 0, \quad (62)$$

where

$$\begin{aligned} a_{11} &= - \left(\frac{1}{k_0^2} \frac{\partial^2}{\partial z^2} - K^2 \right) \frac{n k_0^2}{k_0^2 \mu_t n - k_t^2 \mu_n} + \frac{k_t^2}{\mu_t} - \epsilon_t \\ a_{12} &= \frac{n k_0^2}{k_0^2 \mu_t n - k_t^2 \mu_n} \left(\frac{1}{k_0} \frac{\partial}{\partial z} + K \right) \left(\kappa_t + \frac{\kappa_n k_t^2}{n k_0^2} \right) + \frac{\kappa_t}{\mu_t} \left(\frac{1}{k_0} \frac{\partial}{\partial z} - K \right) \\ a_{21} &= - \frac{n k_0^2}{k_0^2 \mu_t n - k_t^2 \mu_n} \left(\frac{1}{k_0} \frac{\partial}{\partial z} - K \right) \left(\kappa_t + \frac{\kappa_n k_t^2}{n k_0^2} \right) - \frac{\kappa_t}{\mu_t} \left(\frac{1}{k_0} \frac{\partial}{\partial z} + K \right) \\ a_{22} &= - \frac{1}{\mu_t} \left(\frac{1}{k_0^2} \frac{\partial^2}{\partial z^2} - K^2 \right) \left(\kappa_t + \frac{\kappa_n k_t^2}{n k_0^2} \right)^2 \frac{n k_0^2}{k_0^2 \mu_t n - k_t^2 \mu_n} + \frac{\kappa_t^2 \epsilon_n}{\mu_0^2 n} - \epsilon_t, \end{aligned} \quad (63)$$

with $n = \epsilon_n \mu_n - \kappa_n^2$.

Assuming a plane wave solution with the longitudinal (z -axis) spatial dependence $\exp(-j\beta z)$ and equating the determinant of (62) to zero leads to the dispersion relation (pages 175 and 176 of Ref. [17])

$$(\beta^2 + K^2)^2 - 2(\beta^2 + K^2) \left[\epsilon_t \mu_t + \kappa_t^2 + \frac{\kappa_t \kappa_n}{n} k_t^2 - \frac{1}{2n} (\epsilon_t \mu_n + \epsilon_n \mu_t) k_t^2 \right] + \epsilon_t \mu_t n_t - n_t \left(\kappa_t + \frac{\kappa_n}{n} k_t^2 \right)^2 + 4K^2 \kappa \left(\kappa + \frac{\kappa_n}{n} k_t^2 \right) - \frac{n_t}{n} (\epsilon_t \mu_n + \epsilon_n \mu_t) k_t^2 + \frac{\epsilon_n \mu_n n_t}{n^2} k_t^4 = 0 \quad , \quad (64)$$

where $k_t^2 = k_x^2 + k_y^2$ and $n_t = \epsilon_t \mu_t - \kappa_t^2$. Equation (64) can be solved for β , giving [17]

$$\frac{\beta^2}{k_0^2} = \epsilon_t \mu_t + \kappa_t^2 - K^2 + \left(\kappa_t \kappa_n - \frac{1}{2} (\epsilon_t \mu_n + \epsilon_n \mu_t) \right) \frac{k_t^2}{n k_0^2} \pm \sqrt{D}, \quad (65)$$

where $\text{Re}[\sqrt{D}] > 0$ and

$$D = \frac{k_t^4}{4n^2 k_0^4} (\epsilon_t \mu_n - \epsilon_n \mu_t)^2 + \kappa_t^2 \epsilon_n \mu_n \frac{k_t^4}{n^2 k_0^4} - \kappa_t \frac{k_t^2}{n k_0^2} \left(2\kappa_t + \kappa_n \frac{k_t^2}{n k_0^2} (\epsilon_t \mu_n + \epsilon_n \mu_t) \right) - 4K^2 \kappa_t \left(\kappa_t + \kappa_n \frac{k_t^2}{n k_0^2} \right) + \epsilon_t \mu_t \left(2\kappa_t + \kappa_n \frac{k_t^2}{n k_0^2} \right) \quad . \quad (66)$$

After solving (65) for the propagation constant β , the ellipticities (ratio of the transverse field components) can be found from (62). Note that in finding $\beta = \beta' + j\beta''$ from (65), the sign choices need to be carefully investigated based on causality (Kramers-Kronig relations) and decay of the Poynting vector for a passive material.

-
- [1] P. R. Bandaru, C. Daraio, K. Yang, and A. M. Rao. A plausible mechanism for the evolution of helical forms in nanostructure growth. *J. Appl. Phys.*, 101:094307, 2007.
 - [2] J. H. Changa and W. Park. Nano elastic memory using carbon nanocoils. *J. Nanobiotechnology*, 3(1):30–35, 2006.
 - [3] C. Daraio, V. F. Nesterenko, S. Jin, W. Wang, and A. M. Rao. Impact response by a foamlike forest of coiled carbon nanotubes. *J. Appl. Phys.*, 100:064309, 2006.
 - [4] M. Fujii, M. Matsui, S. Motojima, and Y. Hishikawa. Magnetoresistance in carbon micro-coils annealed at various temperatures. *J. Cryst. Growth*, 237-239:1937–1941, apr 2002.
 - [5] F. J Garcia-Vidal. Metamaterials: towards the dark side. *Nat. Photon*, 2(4):215–216, 2008.
 - [6] M. Homma, M. Konyo, T. Maeno, and S. Motojima. Analysis of static and dynamic characteristics of a tactile sensor using carbon micro coil inside an elastic material. *Proceedings*

- of the 2006 IEEE/RSJ International Conference on Intelligent Robots and Systems, pages 1933–1938, oct 2006.
- [7] J.-M. Jin. *Theory and Computation of Electromagnetic Fields*. Wiley-IEEE Press, 2011.
 - [8] J. A. Kong. *Electromagnetic Wave Theory*. EMW Publishing, 2005.
 - [9] C. Kuzuya, Y. Hishikawa, and S. Motojima. Preparation of carbon micro-coils by ultrasonic wave cvd. *J. Chem. Eng. Jpn.*, 35(2):144–149, 2002.
 - [10] C. Kuzuya, W. In-Hwang, S. Hirako, Y. Hishikawa, and S. Motojima. Preparation, morphology, and growth mechanism of carbon nanocoils. *Chem. Vap. Deposition*, 8(2):57–62, 2002.
 - [11] J. Liu, S. Webster, and D. L. Carroll. Highly aligned coiled nitrogen-doped carbon nanotubes synthesized by injection-assisted chemical vapor deposition. *J. Appl. Phys.*, 88:213119, 2006.
 - [12] A. Ludwig and K. J Webb. Accuracy of effective medium parameter extraction procedures for optical metamaterials. *Phys. Rev. B*, 81(11):113103, 2010.
 - [13] A. M. Nicolson and G. F. Ross. Measurement of the intrinsic properties of materials by time-domain techniques. *Instrumentation and Measurement, IEEE Transactions on*, 19(4):377–382, 1970.
 - [14] A. Ozasa, K. Nakamatsul, R. Kometanil, T. Hoshino, K. Kandal, Y. Haruyama, J. Fujita, T. Kaito, and S. Matsuil. Electromagnetic induction phenomena of nano-coil fabricated by fib-cvd. *Microprocesses and Nanotechnology Conference, 2005 International*, pages 222– 223, oct 2005.
 - [15] J. B. Pendry. A chiral route to negative refraction. *Science*, 306:1353–1355, 2004.
 - [16] E. Plum, J. Zhou, J. Dong, V. A. Fedotov, T. Koschny, C. M. Soukoulis, and N. I. Zheludev. Metamaterial with negative index due to chirality. *Phys. Rev. B*, 79:035407, 2009.
 - [17] A. Serdyukov, I. Semchenko, S. Tretyakov, and A. Sihvola. *Electromagnetics of Bi-anisotropic Materials: Theory and Applications*, volume 11 of *Electrocomponent Science Monographs*. Gordon and Breach Science Publishers, Amsterdam, 2001.
 - [18] A. Sihvola. *Electromagnetic Mixing Formulae and Applications*, volume 47 of *Electromagnetic Waves Series*. IEE Publishing, London, 1999.
 - [19] D. R. Smith, S. Schultz, P. Markoš, and C. M. Soukoulis. Determination of effective permittivity and permeability of metamaterials from reflection and transmission coefficients. *Phys. Rev. B*, 65:195104, 2002.

- [20] S. Tretyakov, I. Nefedov, A. Sihvola, S. Maslovski, and C. Simovski. Metamaterial with negative index due to chirality. *J. Electromagn. Waves and Appl.*, 17(5):695–706, 2003.
- [21] S. Tretyakov, A. Sihvola, and L. Jylha. Backward-wave regime and negative refraction in chiral composites. *Photonics and Nanostructures*, 3:107–115, 2005.
- [22] V.K. Varadan and J. Xie. Synthesis of carbon nanocoils by microwave cvd. *Smart Mater. Struct.*, 11:728–734, 2002.
- [23] W. Wang and A. M. Rao. Bulk synthesis of helical coiled carbon nanostructures. *Mater. Res. Soc. Symp. Proc.*, 858E:HH.2.8.1, oct 2005.
- [24] W. Wang, K. Yang, J. Gaillard, P. R. Bandaru, and A. M. Rao. Rational synthesis of helically coiled carbon nanowires and nanotubes through the use of tin and indium catalysts. *Adv. Mater.*, 20:179–182, 2008.
- [25] S. Yang, X. Chen, and S. Motojima. Tactile sensing properties of protein-like single-helix carbon microcoils. *Carbon*, 44(15):3352–3355, dec 2006.